

LINE-OF-SIGHT VELOCITY AND METALLICITY MEASUREMENTS OF THE PALOMAR 5 TIDAL STREAM

M. N. ISHIGAKI¹

Kavli Institute for the Physics and Mathematics of the Universe (WPI), The University of Tokyo, Kashiwa, Chiba 277-8583, Japan

N. HWANG²

Korea Astronomy and Space Science Institute, 776 Daedeokdae-Ro Yuseong-Gu, Daejeon 34055, Korea

M. CHIBA³

Astronomical Institute, Tohoku University, Aoba-ku, Sendai 980-8578, Japan

AND

W. AOKI⁴

National Astronomical Observatory of Japan, 2-21-1 Osawa, Mitaka-shi, Tokyo 181-8588, Japan

ABSTRACT

We present Subaru/FOCAS and Keck/DEIMOS medium-resolution spectroscopy of a tidally disrupting Milky Way (MW) globular cluster Palomar 5 and its tidal stream. The observed fields are located to cover an angular extent of $\sim 17^\circ$ along the stream, providing an opportunity to investigate a trend in line-of-sight velocities (V_{los}) along the stream, which is essential to constrain its orbit and underlying gravitational potential of the Milky Way's dark matter halo. A spectral fitting technique is applied to the observed spectra to obtain stellar parameters and metallicities ($[\text{Fe}/\text{H}]$) of the target stars. The 19 stars most likely belonging to the central Pal 5 cluster have a mean V_{los} of -58.1 ± 0.7 km s⁻¹ and metallicity $[\text{Fe}/\text{H}] = -1.35 \pm 0.06$ dex, both of which are in good agreement with those derived in previous high-resolution spectroscopic studies. Assuming that the stream stars have the same $[\text{Fe}/\text{H}]$ as the progenitor cluster, the derived $[\text{Fe}/\text{H}]$ and V_{los} values are used to estimate the possible V_{los} range of the member stars at each location along the stream. Because of the heavy contamination of the field MW stars, estimated V_{los} range depends on prior assumptions about the stream's V_{los} , which highlights the importance of more definitely identifying the member stars using proper motion and chemical abundances to obtain an unbiased information of V_{los} in the outer part of the Pal 5 stream. The models for the gravitational potential of the MW's dark matter halo that are compatible with the estimated V_{los} range are discussed.

Subject headings: Galaxy: globular clusters: individual: Palomar 5 – stars: abundances – stars: kinematics and dynamics

1. INTRODUCTION

A stellar tidal stream associated with a globular cluster Palomar 5 (Pal 5) is considered as one of the sensitive probes of both the global structure and the substructures of the dark matter halo of the Milky Way (MW) Galaxy (Küpper et al. 2015, and reference therein). While streams are now known to be ubiquitous in the MW, thanks to the recent wide-field photometric surveys, (e.g. Ibata et al. 1994; Grillmair 2006; Grillmair & Dionatos 2006b; Belokurov et al. 2007; Bonaca et al. 2012; Bernard et al. 2014), Pal 5 stream is considered as one of the ideal objects as a tracer of the MW's gravitational potential in the outer stellar halo in many respects. Most importantly, the Pal 5 stream has a long and thin morphology (Odenkirchen et al. 2003; Grillmair & Dionatos 2006c), which is useful to reconstruct the progenitor's orbit. (e.g. Eyre & Binney 2009; Koposov et al. 2010). Another important property of the Pal 5 stream is that its progenitor is clearly identified as a globular cluster in the MW halo at a distance of ~ 23 kpc from the Sun. This offers an opportunity to investigate mechanisms of tidal disruption and resulting formation of tidal streams in great detail (e.g. Dehnen et al. 2004; Küpper et al. 2012; Bovy 2014). It has also been sug-

gested that stellar density fluctuations along a thin tidal stream like the Pal 5 stream are the signature of past interactions with numerous invisible dark matter subhalos expected to present according to the cold dark matter model (e.g. Yoon et al. 2011; Carlberg et al. 2012). Detailed analyses of possible signatures of the density fluctuation along the Pal 5 stream have provided implications on the degree of substructures in the MW's dark matter halo (Carlberg et al. 2012; Ibata et al. 2015; Ngan & Carlberg 2015).

In order to make a stringent constraint on the structure/substructures of the MW's dark matter halo using stellar streams, information on kinematics (i.e. line-of-sight velocities and proper motions) is crucial. While the kinematic properties of the progenitor Pal 5 cluster and its neighboring tidal tails have been reported, (Odenkirchen et al. 2002; Fritz & Kallivayalil 2015; Odenkirchen et al. 2009), little is known on the kinematics of the outer part of the stream, which is crucial for making better constraints on the dark matter halo structure.

One important difficulty in obtaining kinematics of the stream comes from the fact that it is difficult to unambiguously identify individual stars belonging to the

stream (Odenkirchen et al. 2009; Kuzma et al. 2015). Since the progenitor cluster has relatively low mass ($\sim 6 \times 10^3 M_\odot$, Odenkirchen et al. 2002) even at its earlier times (at most ~ 10 times more massive than present days, Odenkirchen et al. 2003; Dehnen et al. 2004), stars are sparsely populated on the tidal stream, especially for the red giant branch (RGB) stars that are bright enough for spectroscopic observations (Koch et al. 2004).

Odenkirchen et al. (2009) used the line profile of the Mg b triplet feature around 5180 Å based on a high-resolution spectroscopy of photometrically pre-selected stars to separate RGB stars from contaminating nearby dwarf stars identifying 17 stars likely belonging to the stream over an angular extent of $\sim 8.5^\circ$. Kuzma et al. (2015) identified the member stars over a larger angular extent of $\sim 20^\circ$, using the equivalent widths of Ca II triplet absorption line from modest resolution spectra and assuming that the line-of-sight velocity of the stream stars to be in a range -70 to -35 km s $^{-1}$.

To improve the accuracy of the membership identification, it is required to first make use of RGB stars much fainter than the horizontal branch ($r < 18$), for which neither the Mg b method nor the Ca T EWs method are generally applicable. It is also important to select the candidate member stars not heavily relying on the line-of-sight velocities since those of the stream stars and the progenitor cluster are not necessarily similar to each other, especially at the stream's outskirts. It has been demonstrated that when the underlying gravitational potential is not spherical or not smooth, the outskirts of the stream would have larger velocity dispersion than expected from a kinematically cold stream (e.g. Yoon et al. 2011; Bonaca et al. 2014; Pearson et al. 2015; Ngan et al. 2016). Therefore, in order to obtain unbiased estimate of kinematics of the whole stream, it is desirable to assign membership using information independent of the line-of-sight velocity, making use of e.g. stellar surface chemical composition.

In this paper, we present medium-resolution multi-object spectroscopy of the Pal 5 cluster and its tidal stream. Our data covers an angular extent of $\sim 17^\circ$ along the stream, which is suitable to evaluate the line-of-sight velocity gradient along the stream. A spectral fitting method is applied to estimate metallicity ($[\text{Fe}/\text{H}]$) of stars. The measured line-of-sight velocity and $[\text{Fe}/\text{H}]$ values are then used to make inference of the line-of-sight velocity at each location of the stream, taking into account contamination from field MW stars. While the present data is not large enough to make strong constraint on the line-of-sight velocity on the outskirts of the Pal 5 stream given a heavy contamination of field stars, the method can be applied to future spectroscopic surveys with next-generation multi-object spectrographs mounted on large (8-10m-class) telescopes.

Section 2 describes the target selection and our Subaru/FOCAS and Keck/DEIMOS observations for the Pal 5 system. Section 3 describes the method we used to measure V_{los} and stellar atmospheric parameters. Section 4 presents the results of the V_{los} and $[\text{Fe}/\text{H}]$ measurement and how these values are used to estimate probable ranges of V_{los} along the longitudinal position in the stream. Section 5 discusses implications on the Galactic potential.

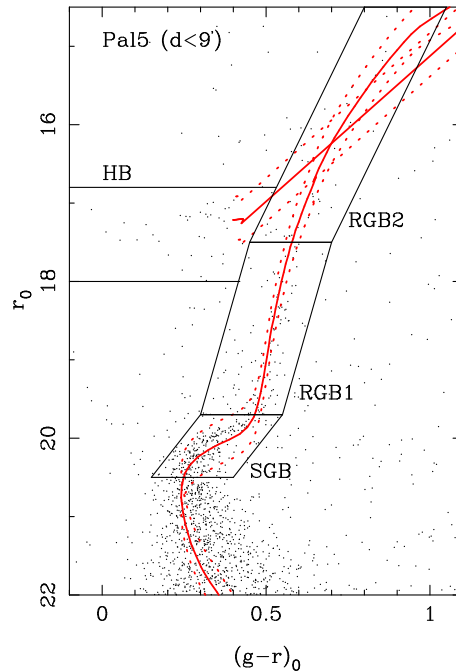


Figure 1. Color-magnitude diagram of the Pal 5 central cluster. The four selection boxes used to select the target fields (RGB1, RGB2, SGB, and HB) are indicated. Isochrones with an age 11 Gyr and $[\text{Fe}/\text{H}] = -1.3$ (Chen et al. 2015) are overlaid with varying distances to the Pal 5 cluster, 23.5 ± 3 kpc.

2. OBSERVATION AND DATA REDUCTION

2.1. Target fields

Target fields along the Pal 5 stream are selected based on the stellar number density of the color-magnitude selected sample using the SDSS g and r photometry (Abazajian et al. 2009). We first defined regions in a color-magnitude diagram (CMD) for stars within $9'$ from the center of Pal 5. The four selection boxes, RGB1, RGB2, HB and SGB, together with theoretical isochrones for an age 11 Gyr, $[\text{Fe}/\text{H}] = -1.3$ and distances 23.5 ± 3 kpc are indicated in Figure 1. Then, locations along the Pal 5 stream at which the number density of the CMD-selected stars is maximized are identified. The resulting positions of the target fields are indicated in Figure 2. Grillmair & Dionatos (2006c) suggests that the distance to stream positions vary from 23.2 kpc at the cluster to 23.9 kpc at apogalacticon, which corresponds to magnitude difference of 0.06 mag. This variation does not significantly affect our CMD selection methods defined based on stars in the Pal 5 central cluster.

The observations were carried out using the Faint Object Camera and Spectrograph (FOCAS) on the Subaru telescope (Kashikawa et al. 2002) and the Deep Imaging Multi-Object Spectrometer (DEIMOS; Faber et al. (2003)) on the Keck II telescope. In both spectroscopic observations, the higher priority was given to stars in the four CMD selection boxes. Most of the other stars with $r < 20.5$ were also observed in the case of the Keck/DEIMOS observation. In the following subsections, we describe details of the observations and the line-of-sight velocity measurements.

2.2. Subaru/FOCAS observation

The Subaru/FOCAS observations were carried out on 29th and 30th of June 2011. The high dispersion VPH grism VPH800, which covers a wavelength range $\sim 7600 - 8600 \text{ \AA}$, was used with a spectral resolution of $R \sim 7000$. The central cluster and its outskirts were covered with 5 pointings (CE1, CE2, NE1, NE2, and SW2). Other pointings were targeted at the stream fields (ST2, ST3, ST4, ST6, and ST7). Locations of the fields are shown in Figure 2. Spectra of metal-poor standard stars with known line-of-sight velocities (HD 186478, BD-18 5550, BD-17°6036, BD+41°3931, HD 111721, HD 117936, and HD 154635) were also obtained for the velocity calibration with the same grating as the target objects. For the raw images, distortion calibration, bias subtraction and flat fielding are performed with the FOCASRED package. Then standard IRAF routines are used for the wavelength calibration using OH skylines and the background sky subtraction. The derived one-dimensional spectra are then normalized by fitting a polynomial to the continuum.

The helio-centric line-of-sight velocities and their associated errors of the target stars are computed by cross-correlating spectra of the target stars with those of the metal-poor standard stars using the IRAF *fxcor* task. Since the field of view ($6'$ diameter) and the number of observed stars are small for the Subaru/FOCAS observations, only the data for the central part of Pal 5 cluster (CE1 and CE2) are mainly used in the following analyses. The details of the observations and the number of stars in each field are summarized in Table 1.

2.3. Keck/DEIMOS observation

The Keck/DEIMOS observation was carried out on 12th and 13th of May 2013. For the spectroscopic observation, the 1200 lines mm^{-1} grating was used together with the OG550 filter, which approximately covers the wavelength range $\sim 6500 - 9000 \text{ \AA}$. The slit width of $0''.75$ was adopted which yields a spectral resolution of $R \sim 6000$. Data reduction was performed by the *spec2d* DEIMOS DEEP2 reduction pipeline (Newman et al. 2013; Cooper et al. 2012). The reduced one-dimensional spectra are finally normalized by fitting a polynomial to the continuum.

The helio-centric line-of-sight velocities and their errors are measured by cross correlating the observed spectra with a synthetic spectrum for a metal-poor giant star with $T_{\text{eff}} = 4500 \text{ K}$, $\log g = 2.5$, $[\text{Fe}/\text{H}] = -1.5$, and $[\alpha/\text{Fe}] = 0.4$ using the IRAF *xcsao* task. In the following analysis, objects with spectra with $\text{S/N} > 10$ and V_{los} error $< 10 \text{ km s}^{-1}$ are used, which amounts to 551 stars in the 10 DEIMOS fields. The observing details and the number of stars in each field are summarized in Table 2.

In the DEIMOS fields one star (FD3-008) is observed in common with Kuzma et al. (2015) (P1238216). The line-of-sight velocity for this object obtained in this work is $-60.6 \pm 8.7 \text{ km s}^{-1}$, which is in good agreement with that obtained by Kuzma et al. (2015) (-59.8 km s^{-1}).

3. ANALYSIS

After correcting for the redshift adopting the estimated line-of-sight velocity, stellar atmospheric parameters and chemical compositions (T_{eff} , $\log g$, $[\text{Fe}/\text{H}]$, and $[\alpha/\text{Fe}]$) are obtained by the following procedure:

(1) Effective temperatures (T_{eff}) are estimated based on the SDSS photometric data by using calibration of Ramírez & Meléndez (2005), initially assuming $[\text{Fe}/\text{H}] = -1.5$.

(2) Synthetic spectra approximated by the Eq. (1) below is fitted with a continuum level, $\log g$, $[\text{Fe}/\text{H}]$ and $[\alpha/\text{Fe}]$ as free parameters. The values of V_{los} and T_{eff} are also allowed to vary within $\pm V_{\text{los}}$ errors and $\pm 50 \text{ K}$, respectively.

(3) Update the value of $[\text{Fe}/\text{H}]$ and repeat (1)-(3) until an approximate convergence ($\lesssim 0.05$ dex in $[\text{Fe}/\text{H}]$) is reached.

Details of the each step are described below.

3.1. Effective temperature

The initial values of T_{eff} are obtained based on the extinction-corrected SDSS ($g - r$) color, which is transformed to the Johnson ($V - R$) color (Jordi et al. 2006). Calibrations of Ramírez & Meléndez (2005) for dwarf and giant stars are used to estimate T_{eff} for each case initially assuming $[\text{Fe}/\text{H}] = -1.5$. The T_{eff} values estimated from the dwarf and giant calibrations are averaged to obtain the T_{eff} used in the following step. The $[\text{Fe}/\text{H}]$ value and dwarf/giant classification used to estimate the T_{eff} are iteratively updated within $\pm 50 \text{ K}$ of the initial value in subsequent steps to obtain a final value of T_{eff} .

3.2. $\log g$, $[\text{Fe}/\text{H}]$, and $[\alpha/\text{Fe}]$

Using the V_{los} and T_{eff} values obtained in the above, we fit the observed spectra with synthetic spectra that are expressed as functions of line-of-sight velocity, continuum level, stellar atmospheric parameters and chemical abundances (iron and α -elements). In the following subsections, we describe the construction of the synthetic spectra.

3.2.1. Construction of the synthetic spectra

We first calculate a grid of synthetic spectra for $T_{\text{eff}} = 4000 - 6250 \text{ K}$, $\log g = 0.2 - 5.0$ dex, $\xi = 0.5 - 2.5 \text{ km s}^{-1}$, $[\text{Fe}/\text{H}] = -2.5 \sim -0.1$, $[\alpha/\text{Fe}] = -0.3 \sim 1.5$, with steps of 250 K , 0.2 dex, 0.5 km s^{-1} , 0.2 dex and 0.3 dex, respectively. For the spectral synthesis calculation, the LTE abundance analysis code used in Aoki et al. (2009) is employed with the Kurucz model atmosphere (Castelli & Kurucz 2004) and linelists of Kurucz (2011). We convolved the theoretical model spectra to make it $R 6000$ and $R 7000$ to compare with FOCAS and DEIMOS spectra, respectively, when the spectral fitting is performed.

Example synthetic spectra with three different metallicities ($[\text{Fe}/\text{H}] = -0.7, -1.3$ and -1.9) and the other stellar parameters of $T_{\text{eff}} = 5000 \text{ K}$, $\log g = 3.0$, and $[\alpha/\text{Fe}] = 0.3$ are shown in Figure 3. The spectral region used in the fitting includes absorption features of Fe-peak (Cr and Ni) and α -elements (Mg, Si, Ca, and Ti) that together constrain $[\text{Fe}/\text{H}]$. The synthetic spectrum for the case of $[\text{Fe}/\text{H}] = -1.3$ is compared with that calculated in Kirby (2011) with the same stellar parameters. These are in good agreement except for molecular features (e.g. CN, C_2) that are not included in this work. Since the molecular features are generally weak compared to the typical noise level in the spectra used in the present work, this would have negligible effects on the parameter determination.

Table 1
Summary of Subaru/FOCAS observation.

Field name	RA	DEC	Date	Exp. time	N_{slits}
CE1	15:15:49.99	-00:09:36.00	29-6-2011	900×4	21
CE2	15:16:05.49	-00:04:48.20	29-6-2011	900×4	26
NE1	15:16:21.51	00:00:07.00	29-6-2011	900×4	10
NE2	15:16:50.48	00:08:51.20	30-6-2011	900×4	8
SW2	15:15:20.53	-00:18:21.40	29-6-2011	900×4	10
ST2	15:20:13.14	00:54:54.30	30-6-2011	900×4	9
ST3	15:24:31.45	01:45:57.00	30-6-2011	900×4	9
ST4	15:28:05.00	02:20:12.50	30-6-2011	900×4	8
ST6	15:59:49.21	05:42:15.60	29-6-2011	900×4	9
ST7	16:07:55.94	06:43:25.70	30-6-2011	900×4	9

Table 2
Summary of Keck/DEIMOS observation.

Field name	RA	DEC	Date (UT)	Exp. time	N_{slits}
FD1	15:09:16.01	-2:02:46.8	13-05-2013	1800×3	103
FD2	15:11:31.46	-1:17:50.8	12-05-2013	1800×3	81
FD3	15:14:13.84	-0:43:30.7	13-05-2013	1800×3	96
FD4	15:14:44.11	-0:12:59.7	12-05-2013	1800×3	78
FD5	15:17:21.87	0:15:36.0	13-05-2013	1800×3	71
FD6	15:22:54.55	1:24:18.9	12-05-2013	1800×3	72
FD7	15:26:51.80	2:09:27.1	13-05-2013	1800×3	71
FD8	15:39:03.08	3:48:22.2	12-05-2013	1800×3	68
FD9	15:50:20.14	4:52:50.8	13-05-2013	1800×3	76
FD10	16:06:27.13	6:28:04.2	12-05-2013	1800×2	87

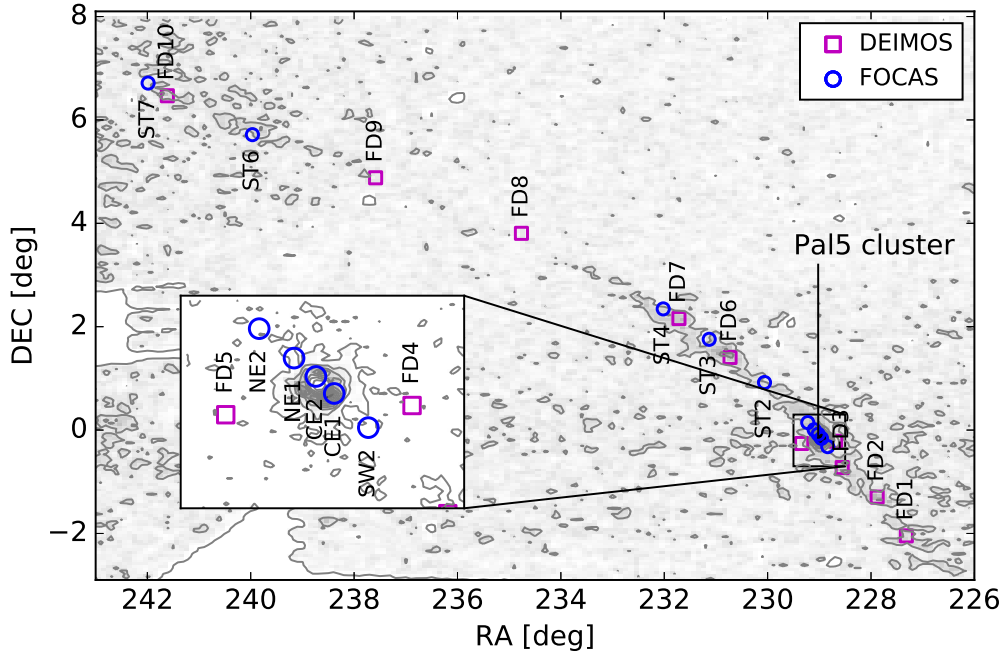


Figure 2. Positions of the target fields marked on the stellar number density diagrams constructed with stars selected in Figure 1. Squares and circles indicate positions of the DEIMOS and FOCAS fields, respectively.

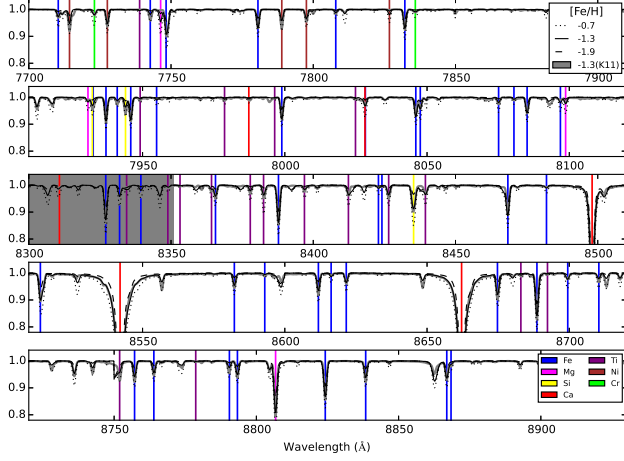


Figure 3. Example of the continuum-normalized synthetic spectra. The thick gray line shows a spectrum from Kirby (2011). Important spectral features to estimate $[\text{Fe}/\text{H}]$ are marked with vertical lines. The region shaded by gray is not used in the spectral fitting because of the heavy contamination with atmospheric absorption.

The grid of synthetic spectra is then, interpolated to obtain formulae that approximate stellar spectra as functions of effective temperature ($\log T_{\text{eff}}$), surface gravity ($\log g$), micro-turbulent velocity (ξ), metallicity ($[\text{Fe}/\text{H}]$), and α -element abundance ($[\alpha/\text{Fe}]$) at each wavelength point as:

$$\begin{aligned}
 f(\log T_{\text{eff}}, \log g, [\text{Fe}/\text{H}], \xi, [\alpha/\text{Fe}]) = & \\
 & a_0 + a_1 \log T_{\text{eff}} + a_2 \log g + a_3 [\text{Fe}/\text{H}] + a_4 \xi + \\
 & a_5 [\alpha/\text{Fe}] + a_6 (\log T_{\text{eff}})^2 + a_7 (\log g)^2 + a_8 [\text{Fe}/\text{H}]^2 + \\
 & a_9 \xi^2 + a_{10} [\alpha/\text{Fe}]^2 + a_{11} \log T_{\text{eff}} \log g + \\
 & a_{12} \log T_{\text{eff}} [\text{Fe}/\text{H}] + a_{13} \log T_{\text{eff}} \xi + \\
 & a_{14} \log T_{\text{eff}} [\alpha/\text{Fe}] + a_{15} \log g [\text{Fe}/\text{H}] + \\
 & a_{16} \log g \xi + a_{17} \log g [\alpha/\text{Fe}] + \\
 & a_{18} [\text{Fe}/\text{H}] \xi + a_{19} [\text{Fe}/\text{H}] [\alpha/\text{Fe}] + a_{20} \xi [\alpha/\text{Fe}] \quad (1)
 \end{aligned}$$

where a_0 - a_{20} are a set of constants for each wavelength point.

At each wavelength point, we fit the normalized flux values with Eq. (1) by an IDL routine *curvefit*, which gives the best-fit values of a_0 - a_{20} at each wavelength.

3.2.2. Spectral fitting

Once the values a_0 - a_{20} have been obtained for the wavelengths in the range 7700 – 8900 Å, we fit the observed spectra with the synthetic spectra with a continuum level, $\log g$, $[\text{Fe}/\text{H}]$, $[\alpha/\text{Fe}]$ as free parameters. In this process, V_{los} and T_{eff} are fixed to the values independently obtained in the process described above within the uncertainties. The ξ is also fixed to the value obtained by an analytic formula which relates $\log g$ and ξ used in Eq. (2) of Kirby et al. (2009). We consider the wavelength range of 7700 – 8900 Å, while available wavelengths vary among the target stars depending on their slit locations in the FOCAS or DEIMOS masks. The wavelength range 8128 – 8351 Å is excluded from the fitting because of the heavy contamination of atmospheric absorption. Cores

of the strong Ca II triplet lines within 1.0 Å are also excluded since departure from the LTE approximation is expected (Kordopatis et al. 2011).

The uncertainties in the $\log g$, $[\text{Fe}/\text{H}]$ and $[\alpha/\text{Fe}]$ obtained by the spectral fitting are evaluated by creating mock spectra for the stellar parameters $T_{\text{eff}} = 5000$ K, $\log g = 3.0$, $[\text{Fe}/\text{H}] = -1.5$, and $[\alpha/\text{Fe}] = 0.3$. For the each case of S/N= 10, 30, and 50, 200 mock spectra are created by adding noises obeying a Gaussian distribution with a σ corresponding to the S/N. In this process, the initial value of T_{eff} is assumed to be known (5000 K) with random errors of a Gaussian with $\sigma = 100$ K. A resulting distribution of the $\log g$ estimated from the 200 mock spectra has a mean of 2.85 dex with a standard deviation of 0.50 dex for the case of S/N= 10. For this S/N, the obtained values of $[\text{Fe}/\text{H}]$ and $[\alpha/\text{Fe}]$ have means of -1.42 and 0.46 dex, with dispersions of 0.14 and 0.17 dex, respectively. The dispersions are smaller for the higher S/N, while the offsets of up to $\Delta[\text{Fe}/\text{H}] = 0.08$ dex and $\Delta[\alpha/\text{Fe}] = 0.18$ dex remain even for the highest S/N case. From this exercise, the internal errors in $[\text{Fe}/\text{H}]$ of at least 0.14 dex should be taken into account. This is much smaller than systematic uncertainties evaluated in the next section.

3.2.3. Comparison with high-resolution spectroscopy

We test the method described above by comparing our estimates of stellar parameters (T_{eff} , $\log g$, $[\text{Fe}/\text{H}]$ and $[\alpha/\text{Fe}]$) with those estimated based on high-resolution spectroscopy ($R \geq 30000$) in literature. In the Subaru/FOCAS observations we took long-slit spectra of two bright metal-poor stars, HD 111721 and HD 186478, for which high-resolution spectroscopic analyses are available from Ishigaki et al. (2012) and Cayrel et al. (2004), respectively. In the Keck/DEIMOS observations, two bright stars FD6-042 and FD6-067 in our sample have been analyzed using high-resolution spectra by Katz et al. (2011). For the comparison, we used four different color- T_{eff} calibrations to estimate initial T_{eff} values adopted in our analysis procedures. The results are summarized in Table 3.

For the four stars used in the comparison, the different color- T_{eff} relations can result in up to ~ 400 K differences in the T_{eff} . These differences lead to a large variation in $\log g$ up to ~ 1 dex, which indicates a strong correlation between T_{eff} and $\log g$ in the analyses adopted in this work. This can be understood as the wavelength range used in the fitting includes only a few significant $\log g$ -sensitive absorption lines. One of the absorption lines within the fitted wavelength range sensitive to $\log g$ for cool ($T_{\text{eff}} \lesssim 5500$ K) stars is the strong Mg I line at 8807 Å, whose pressure-broadened wings are expected for higher $\log g$. This feature is, however, relatively weak for the lower $[\text{Fe}/\text{H}]$ star HD 186478, which likely causes the > 1 dex discrepancy in $\log g$ depending on the adopted T_{eff} values.

On the other hand, the $[\text{Fe}/\text{H}]$ values do not largely depend on the adopted color- T_{eff} scales. For the ($V - R$) color with the Ramírez & Meléndez (2005) scale, which is used for the remaining target stars, the obtained $[\text{Fe}/\text{H}]$ values are in agreement with those derived with the high-resolution spectroscopy within 0.25 dex. These comparisons suggest that systematic uncertainties in the $[\text{Fe}/\text{H}]$ estimates of up to ~ 0.25 dex in stars in a range

$-2.6 < [\text{Fe}/\text{H}] < -0.1$. Because of the relatively large uncertainty in the $\log g$ and $[\alpha/\text{Fe}]$ estimates, we only use $[\text{Fe}/\text{H}]$ to identify candidate stream stars in the following analyses. Precision of the $[\text{Fe}/\text{H}]$ values is further investigated in Section 4.1.

3.3. Proper motion

To exclude objects that unlikely belong to the stream, proper motion of the target stars are obtained from the Initial Gaia Source List (IGSL) (Smart 2013) catalog, when available. We use the proper motion data only if errors in μ_α and μ_δ are both smaller than 50 %.

If the stream is kinematically cold, stars belonging to the stream have a proper motion vector approximately aligned with the projected location of the stream and move toward the direction of motion of the Pal 5 cluster. At each sky position along the stream, we compare proper motion vectors of the target stars (transformed to the Galactic coordinate) with a vector tangent (positive toward increasing $l \cos b$ and b direction) to the stream. The angle (θ) between these vectors should be around $\theta \sim 180^\circ$ or $\cos \theta \sim -1$ if the star belongs to the stream. Therefore, we exclude objects with $\cos \theta > -0.5$ from the candidate stream stars. We also exclude objects with either $\mu_l \cos b > 20$ or $\mu_b > 20$ mas/yr since the proper motion of the Pal 5 has been reported to be much smaller (Fritz & Kallivayalil 2015).

Since the proper motions are either unavailable or subject to large uncertainties for the majority of the target stars, the proper motion criterion has only a minor effect in the selection of the candidate stream stars (see Section 4.2).

4. RESULTS

4.1. Velocity and metallicity of the Pal 5 cluster

Among the stars in the two FOCAS fields covering the central region of the Pal 5 cluster, CE1 and CE2, we select the putative member stars belonging to the Pal 5 central cluster. The selection is made by iteratively eliminating three-sigma outliers of the line-of-sight velocities and the $[\text{Fe}/\text{H}]$ values from the target stars. This process leaves 19 stars that are most likely belonging to the central cluster. The estimated properties of these stars are summarized in Table 4.

For these Pal 5 cluster stars, we first estimate the $[\text{Fe}/\text{H}]$ and $[\alpha/\text{Fe}]$ treating $\log g$ as a free parameter ($\log g_{\text{spec}}$, columns 7-9) as has been done for the rest of the target stars. This results in, however, unrealistic values of $\log g$ for some objects such that the $\log g$ values are not consistent with the distance (23.5 kpc) to the Pal 5 cluster. In order to check the robustness of the $[\text{Fe}/\text{H}]$ estimates against the change in $\log g$, we next estimate the $[\text{Fe}/\text{H}]$ and $[\alpha/\text{Fe}]$ by fixing $\log g$ to the one derived by the standard relation between an apparent magnitude, an effective temperature and a distance ($\log g_{\text{photo}}$, columns 10-12). As can be seen from the Table 4, the spectral fitting method tend to overestimate $\log g$ by 0.9 dex on average. Accordingly, the resulting values of $[\alpha/\text{Fe}]$ in the two methods are different by > 0.5 dex for some of the target stars. On the other hand, the $[\text{Fe}/\text{H}]$ values between the two methods remain similar with a mean difference of $[\text{Fe}/\text{H}](\log g_{\text{spec}}) - [\text{Fe}/\text{H}](\log g_{\text{photo}}) = 0.01$ dex with the standard deviation of 0.18 dex, which is well

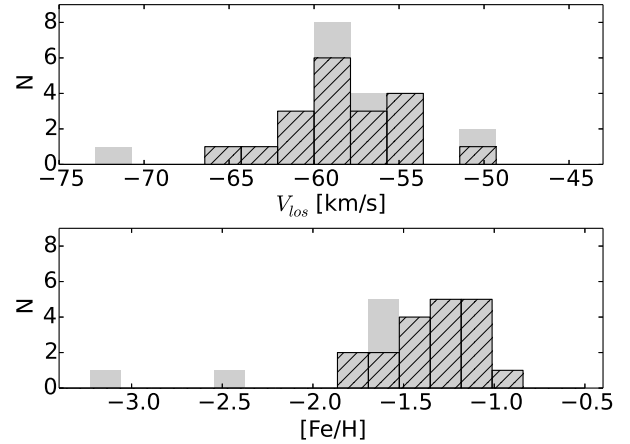


Figure 4. Distribution of the line-of-sight velocities (top) and the $[\text{Fe}/\text{H}]$ values (bottom) for the stars in the central region of Pal 5. Hatched histograms are for stars identified as the Pal 5 cluster members.

within the expected systematic uncertainties. The large uncertainties in $\log g$, therefore, would not significantly affect the stream membership analyses below based solely on the V_{los} and $[\text{Fe}/\text{H}]$ values.

Figure 4 shows the line-of-sight velocity and $[\text{Fe}/\text{H}]$ distributions of stars in the CE1 and CE2 fields. The distributions for the selected member stars are shown in the hatched histograms. Based on these 19 sample stars, a mean V_{los} of the Pal 5 cluster is estimated to be -58.1 ± 0.7 km s $^{-1}$, which is in good agreement with the value obtained by Odenkirchen et al. (2002) (-58.7 ± 0.2 km s $^{-1}$). The line-of-sight velocity dispersion is estimated to be $\sigma_{V_{\text{los}}} = 3.2$ km s $^{-1}$, which is compatible with a typical uncertainty in the V_{los} measurements in this work. This is consistent with a very small intrinsic velocity dispersion of < 1 km s $^{-1}$ obtained by Odenkirchen et al. (2002).

The mean $[\text{Fe}/\text{H}]$ value for the 19 stars is -1.35 ± 0.06 dex, which is also in good agreement with the mean $[\text{Fe}/\text{H}]$ value (~ -1.3) obtained from the high-resolution spectroscopy of four red-giant stars in Pal 5 by Smith et al. (2002). A dispersion in the $[\text{Fe}/\text{H}]$ distribution is $\sigma_{[\text{Fe}/\text{H}]} = 0.25$ dex, which gives a 1σ upper limit on any internal metallicity spread. Since the high-resolution spectroscopy of the cluster members reported a very small $[\text{Fe}/\text{H}]$ spread for Pal 5 (Smith et al. 2002), the $[\text{Fe}/\text{H}]$ dispersion in this work is likely dominated by precisions in our $[\text{Fe}/\text{H}]$ measurements. In the following, we take the value of $\sigma_{[\text{Fe}/\text{H}]} = 0.25$ dex as a typical value for an uncertainty in our $[\text{Fe}/\text{H}]$ measurements.

4.2. Selection of the candidate stream stars

Based on the estimated $[\text{Fe}/\text{H}]$ values, together with the available photometry and proper motion data, we select candidate members of the Pal 5 stream by following criteria:

1. Location in the CMD is close to the locus of the Pal 5's giant/subgiant/horizontal branch (an area surrounded by the solid lines in Fig. 6). The wider color and magnitude ranges than those of the cluster stars are adopted to take into account a possible distance variation along the stream. Adopting

Table 3
Comparison with high-resolution spectroscopy

Star name	parameters	TW ^a					HR ^b
		(V - R)/RM05	(V - I)/RM05	(V - K)/RM05	(V - K)/C10	(V - K)/A99	
HD 111721	T_{eff} (K)	4969	5211	4993	...	4979	4947
	$\log g$	2.8	3.6	2.9	...	2.8	2.63
	[Fe/H]	-1.27	-1.18	-1.25	...	-1.24	-1.33
	[α /Fe]	0.54	0.46	0.52	...	0.52	0.35
HD 186478	T_{eff} (K)	4720	5033	4670	...	4651	4700
	$\log g$	2.3	3.3	2.2	...	2.1	1.3
	[Fe/H]	-2.37	-2.09	-2.43	...	-2.44	-2.59
	[α /Fe]	0.47	0.18	0.51	...	0.53	0.36
FD6-042 (FM5-46436)	T_{eff} (K)	6059	5614	5909	5988	...	5861
	$\log g$	5.0	4.9	5.0	5.0	...	4.23
	[Fe/H]	-0.03	-0.16	-0.08	-0.08	...	0.09
	[α /Fe]	0.06	-0.03	-0.01	0.02
FD6-067 (FM5-49663)	T_{eff} (K)	5752	5508	5908	6028	...	5892
	$\log g$	5.0	4.6	5.0	5.0	...	4.06
	[Fe/H]	-0.91	-0.94	-0.83	-0.90	...	-0.72
	[α /Fe]	0.04	0.09	0.08	0.20

^a The initial T_{eff} values are obtained using different color/color- T_{eff} calibrations (RM05: Ramírez & Meléndez (2005), C10: Casagrande et al. (2010), and A99: Alonso et al. (1999)). The V, R, I magnitudes are based on Zacharias et al. (2005), Monet et al. (2003), or the SDSS photometry, while the K band magnitudes are taken from the 2MASS catalog Cutri et al. (2003). Other parameters are obtained by fitting synthetic spectra to observed ones.

^b The parameters obtained based on high-resolution spectroscopy from literature. HD 111721: Ishigaki et al. (2012), HD 186478: Cayrel et al. (2004). FD6-042, FD6-067: Katz et al. (2011). The [α /Fe] values given here are obtained by averaging the [Mg/Fe], [Si/Fe], [Ca/Fe], [Ti I/Fe] and [Ti II/Fe] values in these literature.

Table 4
Identified Pal 5 member stars in the FOCAS fields

Field	Star	RA	DEC	V_{los}	T_{eff}	$\log g_{\text{spec}}$			$\log g_{\text{photo}}$			S/N
						$\log g$	[Fe/H]	[α /Fe]	$\log g$	[Fe/H]	[α /Fe]	
		(deg)	(deg)	(km s ⁻¹)	(K)	(dex)	(dex)	(dex)	(dex)	(dex)	(dex)	
CE1	s1	228.99337	-0.14527	-59.7	5400	4.6	-1.36	0.23	3.6	-1.25	0.50	23
CE1	s5	228.98538	-0.14497	-57.6	5700	5.0	-1.00	-0.29	3.8	-1.02	0.08	12
CE1	s6	229.00683	-0.16416	-60.3	5270	4.6	-1.17	-0.06	3.6	-1.08	0.18	21
CE1	s7	229.00375	-0.17778	-56.4	5218	4.9	-1.85	0.25	3.7	-1.47	0.72	11
CE1	s8	228.95590	-0.11171	-55.5	5464	5.0	-1.28	0.12	3.8	-1.13	0.50	29
CE1	s11	228.97464	-0.14002	-55.0	5041	3.1	-1.08	0.37	2.8	-1.12	0.40	40
CE1	s13	228.96814	-0.11985	-54.6	4987	2.9	-1.52	0.64	3.1	-1.52	0.62	24
CE1	s15	228.98008	-0.17857	-51.2	5076	3.7	-1.22	0.50	3.1	-1.20	0.58	20
CE1	s21	229.00542	-0.16097	-62.2	5502	4.3	-1.46	0.26	2.5	-1.71	0.91	14
CE2	s8	229.00142	-0.11537	-59.3	5927	5.0	-1.33	0.20	3.9	-1.61	1.19	13
CE2	s10	229.04567	-0.07553	-59.6	5910	5.0	-1.25	0.13	3.9	-1.60	1.49	22
CE2	s11	229.01102	-0.11853	-58.9	5389	4.5	-1.55	0.03	3.7	-1.51	0.25	19
CE2	s14	229.03761	-0.10854	-60.6	5159	1.8	-1.67	0.34	3.0	-1.46	0.17	41
CE2	s16	228.99309	-0.10317	-56.5	4985	3.3	-1.07	0.30	3.0	-1.10	0.34	30
CE2	s17	229.06385	-0.10081	-60.8	5097	4.0	-1.22	0.36	2.5	-1.29	0.65	10
CE2	s18	229.01076	-0.09384	-58.2	4902	2.4	-1.86	0.32	2.9	-1.79	0.27	13
CE2	s22	229.02013	-0.12284	-65.3	5098	5.0	-1.18	0.01	3.3	-1.09	0.47	12
CE2	s23	228.97912	-0.08659	-58.0	5280	5.0	-1.14	0.18	2.6	-1.12	0.68	22
CE2	s24	229.03326	-0.12798	-54.6	5544	3.9	-1.39	0.52	2.5	-1.75	1.47	11

this criterion leave 248 candidate stars in the 10 DEIMOS fields.

- The estimated [Fe/H] value is consistent with that of the central cluster (-1.35 dex) within 3σ (~ 0.75 dex). This reduces the number of candidate stars to 141.
- The proper motions satisfy the criteria described in Sec. 3.3, if available. Note that stars with proper motion errors $> 50\%$ are not removed by this criterion. As mentioned before, the proper motion is either unavailable or associated with large uncertainties for the majority of the sample stars. As a result, this criterion reduces only $\sim 8\%$ of the stars

selected in the previous steps.

In order to evaluate possible contamination of field MW stars, we use the Besançon model (Robin et al. 2003) to create simulated catalogs of photometry and kinematics for the field stars within 1 deg^2 fields centered at the locations of the each DEIMOS field.

Figure 5 shows line-of-sight velocity distributions for the stars in all of the DEIMOS fields. The V_{los} distribution for the all sample stars ($S/N > 10$, V_{los} error $< 10 \text{ km s}^{-1}$; the gray histogram) is dominated by the field MW stars and peaked at $\sim -20 \text{ km s}^{-1}$. In the distribution for the sample stars satisfying the criteria 1-3 (the red histogram), the velocity peak dominated by the field

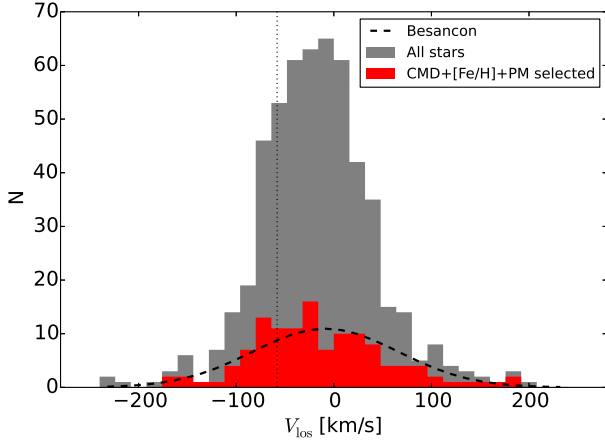


Figure 5. Line-of-sight velocity histograms of the sample stars with $S/N > 10$ in the 10 DEIMOS fields. The gray and red histograms are for all stars and candidate stream stars, respectively. The vertical dotted line corresponds to the velocity of the central cluster (-58.1 km s^{-1}). The dashed line represents the line-of-sight velocity distribution at the direction of FD4 for the field MW stars based on the Besançon model.

stars is suppressed but still remains to be significant.

For comparison, the expected distribution for the field MW stars satisfying the same CMD and $[\text{Fe}/\text{H}]$ criteria (criteria 1 and 2) is shown in the dashed line in Figure 5. The distribution of the field MW stars is peaked at -9 km s^{-1} with dispersion of 77 km s^{-1} . The V_{los} distribution likely representing the stream stars is peaked at $\sim -65 \text{ km s}^{-1}$, which lies within the velocity distribution of the field MW stars, preventing a clean separation of the member stars. If we apply an additional V_{los} cut, $-100 < V_{\text{los}} < -20 \text{ km s}^{-1}$, to minimize contamination from the field MW stars and to be $\pm \sim 40 \text{ km s}^{-1}$ of the V_{los} of the Pal 5 cluster (-58 km s^{-1}), 54 stars remain. Positions, magnitudes, line-of-sight velocities, metallicities and the status of the V_{los} cut for stars satisfying the criteria 1-3 are given in Table 5.

The left panel of Figure 6 shows a CMD of the target stars. The candidate stream stars, which satisfy the criteria 1-3 and have $-100 < V_{\text{los}} < -20 \text{ km s}^{-1}$, are marked as red circles. For a comparison, the right panel shows an expected distribution of the field MW stars around one of the DEIMOS field, FD4, obtained by the Besançon model (Robin et al. 2003).

The major contaminants to the candidate stream stars are the MW field thick disk and halo stars. We estimate the expected number of contaminating stars using the Besançon model by applying the same cuts as the sample stars and scaling the number of stars according to the field-of-view of the DEIMOS mask ($16.7' \times 5'$). Taking into account the fact that our spectroscopic sample with the adopted quality limit ($S/N > 10$ and V_{los} error $< 10 \text{ km s}^{-1}$) amount to 18-44 % of the SDSS photometric sample in the magnitude range $r = 14 - 21$ in the ten DEIMOS fields, the expected number of contaminants is 35 or 40, depending on whether or not the proper motion criteria 3 is applied. This implies that more than half of the 54 candidate stream stars could be contaminants from the field MW stars, while a certain fraction of them could actually belong to the stream.

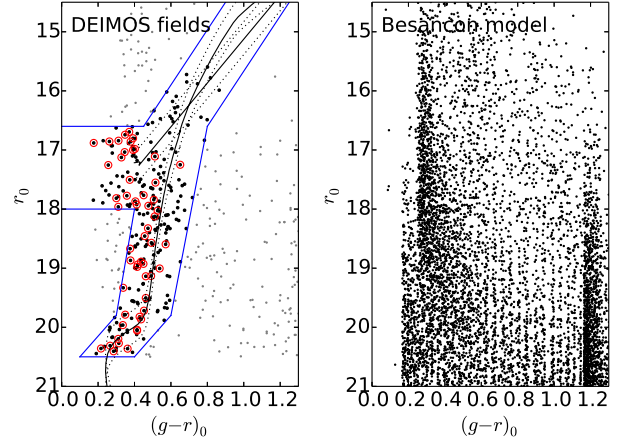


Figure 6. *Left:* The color-magnitude selection box (solid blue) to select candidate member stars. Gray dots indicate all sample stars observed with DEIMOS. Black dots indicate the sample stars satisfying $S/N > 10$, V_{los} error $< 10 \text{ km s}^{-1}$ and the color-magnitude selection criterion. Red open circles mark the candidate stream stars (see text in Section 4.2). Isochrones with an age 11 Gyr and $[\text{Fe}/\text{H}] = -1.3$ (Chen et al. 2015) with varying distances $23.5 \pm 3.0 \text{ kpc}$ are overlaid with black solid and dotted lines. *Right:* Simulated Milky Way foreground stars by Besançon model.

4.3. Individual fields

Figure 7 shows the line-of-sight velocities of the sample stars as a function of $l \cos b$. The gray dots indicate all stars and the black dots indicate stars that satisfy the color-magnitude criterion 1. The open triangles are for objects that fulfill the criteria 1 and 2 but not the criterion 3. Finally, the red circles represent objects that satisfy all of the three criteria. Among them, the objects with $-100 < V_{\text{los}} < -20 \text{ km s}^{-1}$ are shown in filled circles (in the following, we refer these stars as “candidate stars”). The V_{los} distribution of the stars selected by the criteria 1-3 have a wide range of velocities, again suggesting a heavy contamination of field MW star.

The V_{los} distributions of stars that fulfill the criteria 1-3 in each of the DEIMOS fields are shown in Figure 8. These are compared with expected velocity distributions of the contaminating field stars from the Besançon model. By applying similar selection criteria as those adopted for the target stars, the V_{los} distribution for the thick disk stars (blue dotted line) is peaked at $\sim 0 \text{ km s}^{-1}$. The distributions of the halo stars are peaked at negative V_{los} values and thus remains as major contaminants after applying the V_{los} cut. The halo star contamination is especially important at FD8-FD10, in which velocity distribution peaks of the halo stars lie between -60 and -30 km s^{-1} .

After applying the V_{los} cut, although the contaminants may still exist, the candidate stars have larger negative values of V_{los} than the Pal 5 cluster on the leading tail. The more distant field (FD1) has candidate stars with larger negative velocities, which would be consistent with the V_{los} gradient along the leading tail. The candidate stars on the trailing tail, on the other hand have V_{los} with smaller negative velocity than the Pal 5 cluster and show a sign of gradient toward more distant part of the stream, as far as the range $-3 < l \cos b < 5^\circ$ is concerned. For more outer part of the stream (FD8-FD10), the signature of the gradient is ambiguous and some of the candidate

Table 5
Stars selected by the CMD, [Fe/H] and proper motion criteria.

Field	Star	RA (deg)	DEC (deg)	g_0^a (mag)	V_{los} (km s $^{-1}$)	[Fe/H] (dex)	V_{los} cut b
FD1	002	227.30743	-2.0780	20.23	86.0 ± 4.6	-1.08	n
FD1	006	227.25285	-2.0564	17.82	53.6 ± 3.0	-1.08	n
FD1	007	227.29528	-2.0668	17.38	-72.7 ± 1.7	-1.09	y
FD1	008	227.23506	-2.0649	20.69	-68.7 ± 9.2	-1.61	y
FD1	011	227.36408	-2.0007	19.28	16.6 ± 3.3	-1.58	n

Note. — Table 5 is published in its entirety in the electronic edition of the *Astrophysical Journal*. A portion is shown here for guidance regarding its form and content.

^a Extinction-corrected SDSS g -band magnitude.

^b 'y' for an object with V_{los} in a range $-100 < V_{\text{los}} < -20$ km s $^{-1}$, 'n' otherwise.

stars have $V_{\text{los}} < -60$ km s $^{-1}$.

4.4. The V_{los} range for the stream

As mentioned in the previous sections, it is not possible to individually separate genuine stream stars from the field MW stars because of the similarity in both V_{los} and [Fe/H] between the stream and the field stars. In this subsection, we make a statistical inference of likely V_{los} values of the stream at each DEIMOS field, instead of applying the sharp [Fe/H] and V_{los} cuts. We construct a model for line-of-sight velocities and metallicities of the CMD-selected stars (the criterion 1 in Section 4.2 in the each DEIMOS field as a combination of actual stream stars and foreground/background MW stars by the method similar to that applied in Walker & Peñarrubia (2011).

We first assume that, in each of the DEIMOS fields, the stream stars are characterized by a mean line-of-sight velocity (\bar{V}), its intrinsic dispersion (Σ_V) and a fraction f_{st} of the stream stars among the CMD-selected stars. Metallicities of the stream stars are assumed to be identical to that of the central cluster estimated in Section 4.1 within the uncertainty. A likelihood of obtaining a line-of-sight velocity V_i and a metallicity M_i for an i 'th sample star given the model parameters $\Theta = \{\bar{V}, \Sigma_V, f_{\text{st}}\}$, is expressed as,

$$L_i(V_i, M_i|\Theta) = f_{\text{st}} P_{\text{st}}(V_i, M_i) + (1 - f_{\text{st}}) P_{\text{MW}}(V_i, M_i) \quad (2)$$

$P_{\text{st}}(V_i, M_i)$ is a probability of a stream star to have measured line-of-sight velocity and metallicity, V_i and M_i , respectively in each field.

These probabilities are given by:

$$P_{\text{st}}(V_i, M_i) = P_{V,\text{st}}(V_i) P_{M,\text{st}}(M_i) \quad (3)$$

where

$$P_{V,\text{st}}(V_i) = \frac{1}{\sqrt{2\pi(\Sigma_V^2 + \epsilon_{V,i}^2)}} \exp \left[-\frac{1}{2} \frac{(V_i - \bar{V})^2}{\Sigma_V^2 + \epsilon_{V,i}^2} \right]$$

$$P_{M,\text{st}}(M_i) = \frac{1}{\sqrt{2\pi\epsilon_{M,i}^2}} \exp \left[-\frac{1}{2} \frac{(M_i - \bar{M})^2}{\epsilon_{M,i}^2} \right]$$

where $\epsilon_{V,i}$ and $\epsilon_{M,i}$ are the uncertainties in velocity

and metallicity measurements, respectively, and \bar{M} is the metallicity of the Pal 5 cluster.

The corresponding probability for the foreground/background MW stars is expressed as

$$P_{\text{MW}}(V_i, M_i) = (1 - f_2 - f_3) P_1(V_i, M_i) + f_2 P_2(V_i, M_i) + f_3 P_3(V_i, M_i) \quad (4)$$

where

$$P_j(V_i, M_i) = P_{V,j}(V_i) P_{M,j}(M_i) \quad (5)$$

$$P_{V,j}(V_i) = \frac{1}{\sqrt{2\pi(\sigma_{V,j}^2 + \epsilon_{V,i}^2)}} \exp \left(-\frac{1}{2} \frac{(V_i - \bar{V}_j)^2}{(\sigma_{V,j}^2 + \epsilon_{V,i}^2)} \right)$$

$$P_{M,j}(M_i) = \frac{1}{\sqrt{2\pi(\sigma_{M,j}^2 + \epsilon_{M,i}^2)}} \exp \left(-\frac{1}{2} \frac{(M_i - \bar{M}_j)^2}{(\sigma_{M,j}^2 + \epsilon_{M,i}^2)} \right).$$

In the above expressions, $j = 1, 2$, and 3 , correspond to the thin disk, thick disk and halo components, respectively. The mean line-of-sight velocity (\bar{V}_j) and its dispersion ($\sigma_{V,j}$) for each Galactic component as well as f_2 and f_3 are evaluated in advance based on the Besançon model. In this step, the mean metallicity (\bar{M}_j) and dispersions ($\sigma_{M,j}$) are fixed to the values $(\bar{M}_j, \sigma_{M,j}) = (-0.1, 0.2), (-0.8, 0.3), (-1.8, 0.5)$ for the thin disk, thick disk and halo, respectively.

A likelihood for each field k is obtained by multiplying the expressions in (2) for the number of stars (N_k),

$$L = \prod_{i=1}^{N_k} L_i \quad (6)$$

Posterior distributions for the parameter-set Θ given the data $\{V_i, M_i\}_{i=1}^{N_k}$ is expressed as,

$$p(\Theta|\{V_i, M_i\}_{i=1}^{N_k}) \propto L(\{V_i, M_i\}_{i=1}^{N_k}|\Theta) I(\Theta) \quad (7)$$

where $I(\Theta)$ is a prior probability distribution for the parameter set. For the $I(\Theta)$, uniform distributions in the ranges $-100 < \bar{V}_k < -20$ km s $^{-1}$, $0 < \Sigma_{V,k} < 5$ km s $^{-1}$ and $0.0 < f_{\text{st},k} < 0.5$ are adopted, where the former for \bar{V}_k is symmetric around the mean velocity of the Pal 5 cluster (~ -58 km s $^{-1}$) and the latter for $f_{\text{st},k}$ is aimed to cover the likely range of the stream fraction. The Markov-Chain Monte Carlo code, *emcee*,

(Foreman-Mackey et al. 2013) is used to sample the posterior probability distribution. The resulting posterior distributions of \bar{V}_k , marginalized over the $\Sigma_{V,k}$ and $f_{st,k}$, do not always have a well-defined single peak but end up with multiple peaks. The point of 50th percentile and the ranges between the 16th and 84th percentiles in the resulting distributions of V_{los} are shown by red circles and pink rectangles, respectively, in Figure 9.

In the DEIMOS fields at $l \cos b < 5^\circ$, the likely V_{los} values for the stream well overlap with the member stars identified in the previous works (Odenkirchen et al. 2009; Kuzma et al. 2015). In the outer region ($l \cos b > 5^\circ$), FD8 and FD10, the likely V_{los} values for the stream also overlap with the member stars identified by Kuzma et al. (2015) while allowing for lower V_{los} than that expected from an extrapolation of the $l \cos b - V_{los}$ relation found in $l \cos b < 5^\circ$.

We note that the prior assumption about \bar{V}_k is crucial in obtaining the results mentioned above. In order to check the robustness of the result, we repeat the same analyses by relaxing the prior assumptions on the possible value of \bar{V}_k to $-160 < \bar{V}_k < 0 \text{ km s}^{-1}$. The resulting distributions show another peak within a range from $\sim 0 \text{ km s}^{-1}$ at FD8 to -30 km s^{-1} at FD10. These peaks roughly coincide with the peak in the velocity distribution of the thick disk and halo stars (Figure 8). Since the $l \cos b - V_{los}$ trend of that peak is in opposite sense to that expected for the Pal 5 stream, it is less likely to be associated with the stream. We also tests a narrower prior of $-100 < \bar{V}_k < -30 \text{ km s}^{-1}$ to reduce contamination from the field thick disk stars. This results in more negative ranges for the posterior \bar{V}_k distribution in the outer part of the stream, which highlight the importance of the adopted prior on the resulting inference of \bar{V}_k .

The high fraction of field MW stars relative to the stream stars in our sample could be understood as an actual deficiency in relatively bright (higher-mass) stars in the stream as reported by Koch et al. (2004) together with the shallow depth in the present spectroscopic observation (up to $r \sim 20.5$). This situation should be improved with deeper spectroscopic observations that can reach below the main-sequence turn-off, which would significantly increase a fraction of the stream stars relative to the field MW stars.

5. DISCUSSION

5.1. Comparison with previous studies

Line-of-sight velocities based on high-resolution spectroscopy have previously been reported by Odenkirchen et al. (2009) covering an angular extent of $\sim 8.5^\circ$ of the streams. Candidate member stars in the streams are selected based on the Mg b triplet feature around 5180 \AA , which is an indicator of a stellar surface gravity. The line-of-sight velocity distribution of the target stars that are identified as a giant is found to be mostly concentrated in a range -70 to -40 km s^{-1} and peaks at -58 km s^{-1} . The peak velocity is consistent with that of the central cluster, suggesting that these giants are indeed plausible candidate members of the stream. Based on these identified members, they reported a V_{los} gradient of $1.0 \pm 0.4 \text{ km s}^{-1} \text{ deg}^{-1}$ as a function of the Galactic longitude.

The small but non-negligible velocity gradient is sup-

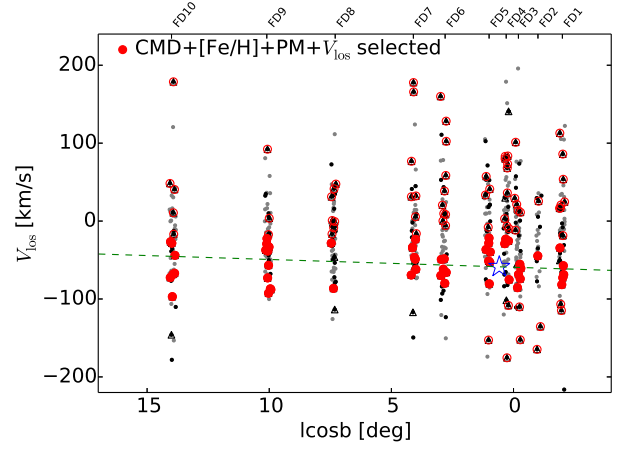


Figure 7. The line-of-sight velocities of the sample stars as a function of $l \cos b$. All stars with $S/N > 10$ are shown in gray dots. Among them, stars satisfying our candidate selection criteria are shown in different symbols: (1) the CMD criterion (black dots), (2) the CMD and $[\text{Fe}/\text{H}]$ criteria (open triangles), (3) the CMD, $[\text{Fe}/\text{H}]$ and proper motion criteria (red circles), among which objects having $-100 < V_{los} < -20 \text{ km s}^{-1}$ are shown in filled red circles. The V_{los} of the central Pal 5 cluster is marked by a star symbol. The dashed line indicates the V_{los} gradient suggested in the previous studies (Odenkirchen et al. 2002; Kuzma et al. 2015).

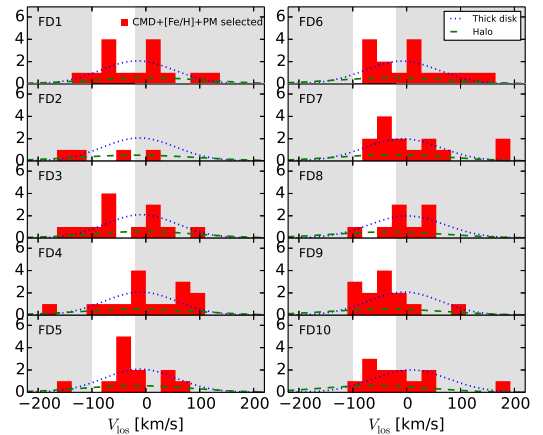


Figure 8. Line-of-sight velocity histograms (red) for stars selected by the criteria (1)-(3) in Section 4.2. The white region corresponds to the V_{los} limit of $-100 < V_{los} < -20 \text{ km s}^{-1}$. The dotted and dashed lines correspond to the velocity distributions (arbitrary vertical scale) for the simulated field thick disk and halo stars, respectively, obtained from the Besançon model.

ported by Kuzma et al. (2015), who have identified candidate member stars over a much larger angular extent. Kuzma et al. (2015) make use of the Ca II triplet absorption lines as a proxy of metallicity ($[\text{Fe}/\text{H}]$) to identify probable member stars. After applying their membership criteria, including the Ca II equivalent widths, dwarf/giant separation, the CMD and the line-of-sight velocities (assumed to be in the range from -70 to -35 km s^{-1}), 47 candidate stars have been identified over an angular extent $\sim 20^\circ$ along the stream. The best-fit linear gradient for these stars is $1.0 \pm 0.1 \text{ km s}^{-1} \text{ deg}^{-1}$, which is in agreement with Odenkirchen et al. (2009).

As mentioned in the previous section, the likely V_{los}

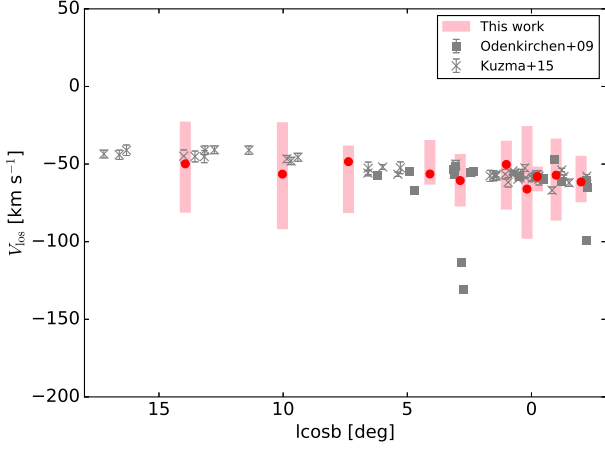


Figure 9. The likely V_{los} ranges for the Pal 5 stream in each DEIMOS field. Red points and pink rectangles correspond to the value of the 50th percentile and the ranges between the 16th and 84th percentiles, respectively, for the posterior distributions of the V_{los} obtained in this work. The V_{los} of candidate member stars identified in Odenkirchen et al. (2009) and Kuzma et al. (2015) are also indicated with squares and crosses, respectively.

range at each stream locations in this work taking into account the contamination of the field stars well overlap with the V_{los} of the member stars identified in Odenkirchen et al. (2009) and Kuzma et al. (2015) for $l \cos b < 5.0^\circ$. For this angular extent, the present result is also compatible with the presence of a gradient suggested by their studies.

In the more outer part of the trailing stream (FD8-FD10), the V_{los} ranges also overlap with those of the identified member stars in Kuzma et al. (2015), while they allow lower V_{los} values for the stream such that $V_{\text{los}} < -50 \text{ km s}^{-1}$. This result would be explained by either (1) significant contamination of the field stars or (2) deviation in V_{los} of the stream stars from that of the Pal 5 cluster orbit.

In the former case, the small field-of-view of a single DEIMOS exposure might have hampered detection of the genuine member stars. As discussed in Section 4.2, contamination of the field stars of up to $\sim 80\%$ is expected according to the Besançon model and thus it is not surprising that the stars that fulfill the adopted criteria in each DEIMOS field are dominated by the contaminants.

For the latter case, some stars once belonging to the cold part of the stream have gained larger velocity dispersions, resulted from e.g. dynamical interactions with dark matter subhalos, which are presumably ubiquitous according to the currently standard ΛCDM cosmology (e.g. Yoon et al. 2011; Bonaca et al. 2014; Ngan et al. 2016). Yoon et al. (2011) suggests that the interaction with the dark matter subhalos results in change in V_{los} and velocity dispersion along a cold stellar stream, depending on the masses of the interacting dark matter subhalos and frequency of the encounters. As an alternative possibility, Pearson et al. (2015) suggests that the morphology and velocity of a stream like Pal 5 would be significantly modified, if the potential of the MW’s dark matter halo was triaxial like the one suggested by Law & Majewski (2010). It is not clear, however, that whether the possible perturbations to the V_{los} is com-

patible with the observed narrowness in the morphology of the stream. Indeed, Kuzma et al. (2015) suggest that the stream is kinematically cold even in the outer region, which does not support the significant heating.

In order to evaluate presence or absence of significant perturbations on the stream’s line-of-sight velocities, analyses of a larger samples without a strong bias in V_{los} itself are required. Identification of the stream member stars, therefore, using chemical abundances (metallicities) as well as proper motions would be crucial to evaluate the possible dynamical heating experienced by Pal 5.

5.2. Implications for the Galactic potential

In this section, we use the possible V_{los} ranges along the Pal 5 stream obtained in Section 4.4 to investigate models of the MW’s gravitational potential that are compatible with the data.

We assume that the Galactic potential is described as a sum of three components, namely, the bulge, disk and dark halo. We adopt the Hernquist model (Hernquist 1990), axis-symmetric Miyamoto-Nagai potential (Miyamoto & Nagai 1975) and the Navarro-Frenk-White (NFW) profile (Navarro et al. 1997) for the bulge, disk and dark halo components, respectively, as adopted in Küpper et al. (2015).

$$\begin{aligned}
 \Psi_{\text{bulge}}(r) &= -\frac{GM_{\text{bulge}}}{r+a} \\
 r &= \sqrt{x^2 + y^2 + z^2} \\
 \Psi_{\text{disk}}(R, z) &= -\frac{GM_{\text{disk}}}{\sqrt{R^2 + \left(b + \sqrt{z^2 + c^2}\right)^2}} \\
 R &= \sqrt{x^2 + y^2} \\
 \Psi_{\text{halo}}(r) &= -\frac{GM_{\text{halo}}}{r} \ln \left(1 + \frac{r}{r_{\text{halo}}}\right) \\
 r &= \sqrt{R^2 + \frac{z^2}{q_{\text{halo}}^2}}
 \end{aligned} \tag{8}$$

where G is a gravitational constant, with $M_{\text{bulge}} = 3.4 \times 10^{10} M_{\odot}$, $a = 0.7 \text{ kpc}$, $M_{\text{disk}} = 10^{11} M_{\odot}$, $b = 6.5 \text{ kpc}$ and $c = 0.26 \text{ kpc}$.

Position and kinematics of the Pal 5 cluster are adopted mainly from the values derived in recent literature. The distance to the Pal 5 cluster $d_{\text{pal5}} = 23.5 \text{ kpc}$ is adopted from the V band distance modulus based on isochrone fitting to the HST photometric data Dotter et al. (2011). The proper motion of Pal 5 has recently been reported to be $(\mu_{\alpha}, \mu_{\delta}) = (-2.296 \pm 0.186, -2.257 \pm 0.181) \text{ mas yr}^{-1}$ based on combined SDSS and Large Binocular Telescope/Large Binocular Camera data, which span a baseline of 15 years (Fritz & Kallivayalil 2015). To make a comparison with Küpper et al. (2015), we first adopt the proper motions obtained in their work, $(\mu_{\alpha} \cos(\delta), \mu_{\delta}) = (-2.40, -2.38)$, then update these values to the latest estimates of Fritz & Kallivayalil (2015).

For the solar-tangential velocity and the distance from the Galactic center, we adopt $V_{\text{tan}} = V_{\text{LSR}} + V_{\odot} = 255.2$

km s^{-1} and $R_\odot = 8.34$, respectively from Reid et al. (2014). The radial and vertical components of the solar motion is adopted to be $U_\odot = 11.1$ and $W_\odot = 7.3 \text{ km s}^{-1}$, which were derived by Schönrich et al. (2010).

We investigate orbits in the potential described above for various dark halo parameters while fixing the model parameters for the bulge and disk components as well as the solar position and kinematics. Specifically, the dark halo parameters obtained by Küpper et al. (2015) using the previously available V_{los} data of Odenkirchen et al. (2009), with their "Overdensity + Radial Velocities" method ($M_{\text{halo}} = 1.75^{+0.76}_{-0.66} [10^{12} M_\odot]$, $r_{\text{halo}} = 41.8^{+14.5}_{-11.0} [\text{kpc}]$, and $q_{\text{halo}} = 0.84^{+0.27}_{-0.16}$) are considered as a standard set of values. We calculate the orbits by varying one of the M_{halo} , r_{halo} and q_{halo} from the standard set, while the other two are fixed.

Figure 10 shows the resulting orbits for different M_{halo} . The top, middle and the bottom panels show the Galactic latitude (b), V_{los} , and distance from the Sun (s), respectively, as a function of $l \cos b$. As can be seen from the middle panel, the models for $M_{\text{halo}} = 1.75$ (thick gray line) and $1.05 \times 10^{12} M_\odot$ (red dashed line), which correspond to a circular velocity at the solar radius $V_c(R_\odot) = 231$ and 218 km s^{-1} , respectively, lie within the likely V_{los} ranges obtained in this work (pink rectangles). On the other hand the higher M_{halo} value of $2.45 \times 10^{12} M_\odot$ (blue dash-dotted line), which corresponds to $V_c(R_\odot) = 242 \text{ km s}^{-1}$, is incompatible with the data in the outer part of the stream.

Figure 11 shows the orbits calculated varying r_{halo} by $\pm 9 \text{ kpc}$ from the standard value, while the other parameters are fixed. The two models for the larger r_{halo} , which correspond to smaller $V_c(R_\odot)$ values ($\lesssim 231$), are compatible with the estimated V_{los} ranges. On the other hand, the smaller r_{halo} value predicts much higher V_{los} than those suggested in the present analysis.

For the models considered in this work, the changes in q_{halo} by ± 0.3 from the standard value of 0.8 have only a small effect on the V_{los} when other parameters are kept fixed, as shown in Figure 12. Larger changes in q_{halo} would result in significant discrepancy between the predicted and the observed projected locations of the stream as can be seen in the top panel.

Finally, Figure 13 shows the same models as in Figure 10 but with the updated values of proper motion of Pal 5 cluster's obtained by Fritz & Kallivayalil (2015). The absolute values of their best proper motion estimates are slightly smaller by 0.10 and $-0.12 \text{ mas yr}^{-1}$ for $\mu_\alpha \cos \delta$ and μ_δ , respectively, than those adopted above although these estimates are consistent within the uncertainty. As shown in the middle panel, the smallest M_{halo} model, which corresponds to $V_c(R_\odot) = 218 \text{ km s}^{-1}$, is compatible with the V_{los} range, while the $M_{\text{halo}} = 1.75 \times 10^{12} M_\odot$ model is only marginally consistent with the data in the outer-most field on the stream. The V_{los} estimates combined with the updated proper motion data, therefore, are better reproduced with the models with $V_c(R_\odot) < 231 \text{ km s}^{-1}$, for the given choice of other MW parameters. However, as discussed in Fritz & Kallivayalil (2015), the conclusion on the model could also depend on the adopted distance to Pal 5 cluster. Proper motion and distance measurements with improved precision are essential to conclude on whether or

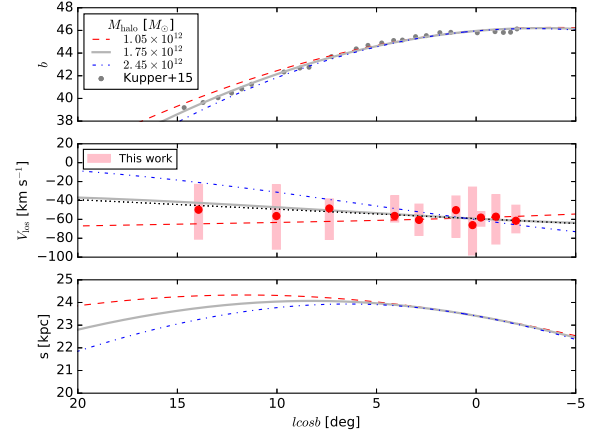


Figure 10. The model orbits calculated based on the parameters estimated by Küpper et al. (2015) (the thick gray line; $M_{\text{halo}} = 1.75 \times 10^{12} M_\odot$) and for different M_h (the red dashed line for $1.05 \times 10^{12} M_\odot$ and blue dash-dotted line for $2.45 \times 10^{12} M_\odot$) are compared with the observed positions (Küpper et al. 2015) and the V_{los} range obtained in this work. The top, middle and bottom panels show Galactic latitude (b), line-of-sight velocities (V_{los}) and distances (s) as functions of Galactic longitude ($l \cos b$). The black dotted line indicates the linear fit to the V_{los} data obtained in Kuzma et al. (2015). The estimated range of V_{los} at each location along the stream are shown with pink rectangles.

not the models with larger M_{halo} are ruled out.

Nevertheless, the preference for the relatively small $V_c(R_\odot)$ is in line with the recent distance estimates by Ibata et al. (2015) along the Pal 5 stream. Their analyses report continuous increase in the distances to the stream from the leading to the trailing tails up to $\sim 10^\circ$ from the Pal 5 cluster. This trend is reproduced with the models with smaller $V_c(R_\odot)$ (either smaller M_{halo} or larger r_{halo}), as shown in the bottom panels in Figure 10, 11 and 13. On the other hand, the models with the larger $V_c(R_\odot)$ values (either $M_{\text{halo}} = 2.45 \times 10^{12} M_\odot$ or $r_{\text{halo}} = 32.8 \text{ kpc}$) predict a turn around in the distance trend at a point closer to the Pal 5 cluster.

To summarize, for the given values for the bulge and disk parameters as well as the solar position and kinematics, the models for the dark matter halo with $V_c(R_\odot) \lesssim 231 \text{ km s}^{-1}$ are consistent with the estimated range for the possible V_{los} values for the Pal 5 stream. This result, however, depends on various factors such as the prior assumption about the V_{los} for the stream and the adopted value for the proper motion of the Pal 5 cluster. The uncertainty in V_{los} primarily comes from the fact that the likely V_{los} and the $[\text{Fe}/\text{H}]$ of the stream members are similar to those for the field MW stars, and thus, with a small sample size, it is difficult to separate the two contributions. Planned and ongoing wide-field and deeper spectroscopic surveys with multi-object capabilities such as LAMOST, WHT/WEAVE, 4MOST, Subaru/PFS would provide chemical compositions and V_{los} together for a large number of stars, which offer an excellent opportunity to better understand the nature of streams and their constraints on the MW's dark matter halo.

6. CONCLUSIONS

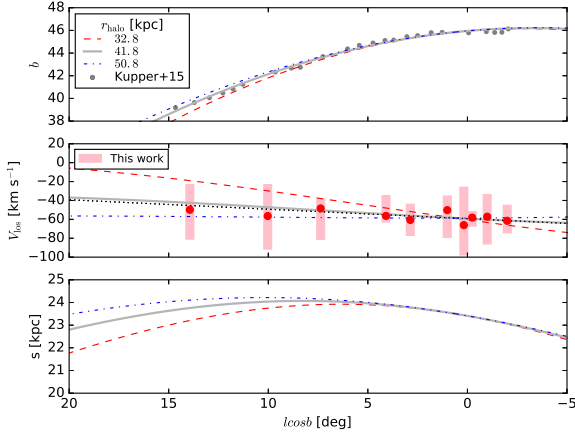


Figure 11. Same as in Figure 10 but for orbits with different r_{halo} (the thick gray line for 41.8 kpc, the red dashed line for 32.8 kpc, and the blue dash-dotted line for 50.8 kpc).

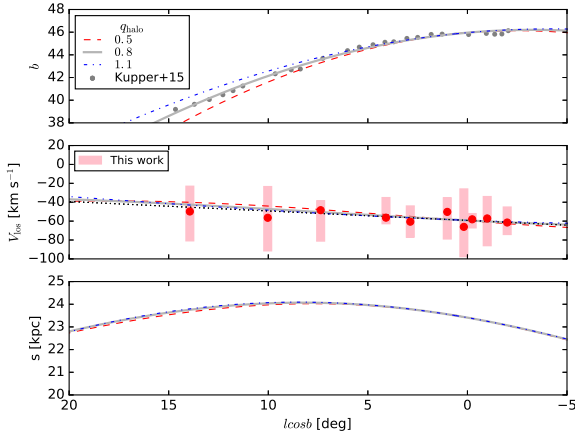


Figure 12. Same as in Figure 10 but for orbits with different q_{halo} (the thick gray line for 0.8, the red dashed line for 0.5, and the blue dash-dotted line for 1.1).

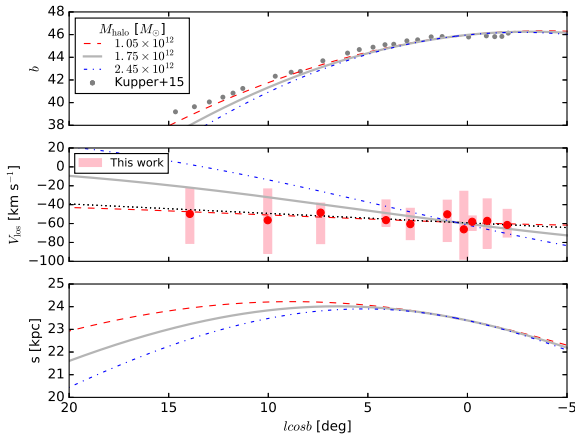


Figure 13. Same as in Figure 10 but for orbits with updated proper motion values from Fritz & Kallivayalil (2015).

We carried out multi-object, medium-resolution spectroscopy along the central cluster and the tidal stream of Pal 5, which enables V_{los} and $[\text{Fe}/\text{H}]$ measurements over an angular extent of $\sim 17^\circ$ along the stream. By adopting the spectral fitting technique to the observed spectra, together with the available SDSS photometry, we derived stellar parameters and $[\text{Fe}/\text{H}]$ of the sample stars. The estimated V_{los} and $[\text{Fe}/\text{H}]$ for the central cluster are $-58.1 \pm 0.7 \text{ km s}^{-1}$ and $[\text{Fe}/\text{H}] = -1.35 \pm 0.06$ dex, respectively, which are in good agreement with that derived in previous high-resolution spectroscopic studies. This value of $[\text{Fe}/\text{H}]$ for the central cluster is used first to identify candidate member stars and second to estimate the range in possible V_{los} of the stream at each projected location along the stream.

The resulting ranges of V_{los} depend on the prior assumptions about V_{los} of the stream because of the overlap in both the expected V_{los} and $[\text{Fe}/\text{H}]$ of the stream with that of the field MW thick disk/halo stars. By assuming the stream V_{los} to be $-100 < V_{\text{los}} < -20 \text{ km s}^{-1}$, the inferred V_{los} range is consistent with previous studies, while it does not exclude the possibility of lower V_{los} at the outer part of the stream. These analyses highlight the importance of more definitely identifying the member stars by using e.g. proper motion and detailed chemical information, in order to obtain unbiased estimates of V_{los} for the entire part of the Pal 5 system. Wider and deeper spectroscopic surveys that provide both V_{los} and chemical compositions for a large number of individual stars would provide important data to better understand the kinematics of the stream, which might eventually put stronger constraint on the nature of the MW's dark matter halo.

The authors are grateful to the referee for his/her constructive comments which helped to improve this paper. We thank T. Hattori and other staff members in Subaru Telescope for their various technical supports in preparing and carrying out our observations. We are also grateful to support astronomers and other staff members of Keck telescope for their generous supports for the observation and data analysis. M.N.I. thank E. Kirby and J. Cohen for their helpful advice on spectroscopic analyses and A. More for helpful discussions during the early stage of this work. M.N.I. acknowledge support through JSPS KAKENHI Grant Number 23740162, 13J07047, and 25-7047.

Funding for the SDSS and SDSS-II has been provided by the Alfred P. Sloan Foundation, the Participating Institutions, the National Science Foundation, the U.S. Department of Energy, the National Aeronautics and Space Administration, the Japanese Monbukagakusho, the Max Planck Society, and the Higher Education Funding Council for England. The SDSS Web Site is <http://www.sdss.org/>.

The SDSS is managed by the Astrophysical Research Consortium for the Participating Institutions. The Participating Institutions are the American Museum of Natural History, Astrophysical Institute Potsdam, University of Basel, University of Cambridge, Case Western Reserve University, University of Chicago, Drexel University, Fermilab, the Institute for Advanced Study, the Japan Participation Group, Johns Hopkins University,

the Joint Institute for Nuclear Astrophysics, the Kavli Institute for Particle Astrophysics and Cosmology, the Korean Scientist Group, the Chinese Academy of Sciences (LAMOST), Los Alamos National Laboratory, the Max-Planck-Institute for Astronomy (MPIA), the Max-Planck-Institute for Astrophysics (MPA), New Mexico State University, Ohio State University, University of Pittsburgh, University of Portsmouth, Princeton University, the United States Naval Observatory, and the University of Washington.

Facilities: Keck (DEIMOS), Subaru (FOCAS).

REFERENCES

- Abazajian, K. N., Adelman-McCarthy, J. K., Agüeros, M. A. et al. 2009, *ApJS*, 182, 543
- Alonso, A., Arribas, S., & Martínez-Roger, C. 1999, *A&AS*, 140, 261
- Aoki, W., Barklem, P. S., Beers, T. C., et al. 2009, *ApJ*, 698, 1803
- Belokurov, V., Evans, N. W., Irwin, M. J., et al. 2007, 658, 337
- Bernard, E. J., Ferguson, A. M. N., Schlafly, E. F., et al. 2014, *MNRAS*, 443, L84
- Bonaca, A., Geha, M., & Kallivayalil, N. 2012, *ApJL*, 760, L6
- Bonaca, A., Geha, M., Küpper, A. H. W. et al. 2014, *ApJ*, 795, 12
- Bovy, J. 2014, *ApJ*, 795, 18
- Carlberg, R. G., Grillmair, C. J., & Hetherington, N. 2012, *ApJ*, 760, 75
- Casagrande, L., Ramírez, I., Meléndez, J., M. Bessell, & Asplund, M. 2010, *A&A*, 512, A54
- Castelli, F., & Kurucz, R. L. 2004, *arXiv:astro-ph/0405087*
- Cayrel, R., Depagne, E., Spite, M., et al. 2004, *A&A*, 416, 1117
- Chen, Y., Bressan, A., Girardi, L., Marigo, P., Kong, X., & Lanza, A. 2015, *MNRAS*, 452, 1068
- Cooper, M. C., Newman, J. A., Davis, M., et al. 2012, *Astrophysics Source Code Library*, record ascl:1203.003
- Cutri, R. M., Skrutskie, M. F., van Dyk, S., et al. 2003, *yCat*, 2246, 0
- Dehnen, W., Odenkirchen, M., Grebel, E. K., & Rix, H.-W. 2004, *AJ*, 127, 2753
- Dotter, A., Sarajedini, A., & Anderson, J. 2011, *ApJ*, 738, 74
- Eyre, A., & Binney, J. 2009, *MNRAS*, 400, 548
- Faber, S. M., Phillips, A. C., Kibrick, R. I., et al., 2003, *SPIE*, 4841, 1657
- Foreman-Mackey, D., Hogg, D. W., Lang, D., & Goodman, J. 2013, *PASP*, 125, 306
- Fritz, T. K., & Kallivayalil, N. 2015, *ApJ*, 811, 123
- Grillmair, C. J. 2006, *ApJ*, 645, L37
- Grillmair, C. J., & Dionatos, O. 2006, *ApJ*, 643, L17
- Grillmair, C. J., Dionatos, O. 2006, *ApJ*, 641, L37
- Jordi, K., Grebe, E. K., Ammon, K. 2006, *A&A*, 460, 339
- Hernquist, L. 1990, *ApJ*, 356, 359
- Ibata, R. A., Gilmore, G., & Irwin, M. J. 1994, *Nature*, 370, 194
- Ibata, R. A., Lewis, G. F., & Martin, N. F. 2015, *arXiv:1512.03054*
- Ishigaki, M. N., Chiba, M. & Aoki, W. 2012, *ApJ*, 753, 64
- Kashikawa, N., Aoki, K., Asai, R., et al., 2002, *PASJ*, 54, 819
- Katz, D., Soubiran, C., Cayrel, R., et al. 2011, *A&A*, 525, 90
- Kirby, E. N., Guhathakurta, P., Bolte, M., Sneden, C. & Geha, M. C. 2009, *ApJ*, 705, 328
- Kirby, E. N. 2011, *yCat*, 6134, 0
- Koch, A., Grebel, E. K., Odenkirchen, M., Martínez-Delgado, D., & Caldwell, J. A. R. 2004, *AJ*, 128, 2274
- Koposov, S. E., Rix, H.-W., & Hogg, D. W. 2010, *ApJ*, 712, 260
- Kordopatis, G., Recio-Blanco, A., de Laverny, P., et al. 2011, *A&A*, 535, A106
- Küpper, A. H. W., Lane, R. R., & Hoggie, D. 2012, *MNRAS*, 420, 2700
- Küpper, A. H. W., Balbinot, E., Bonaca, A. et al. 2015, *ApJ*, 803, 80
- Kurucz, R. L. 2011, *CaJPh*, 89, 417
- Kuzma, P. B., Da Costa, G. S., Keller, S. C., & Maunder, E. 2015, *MNRAS*, 446, 3297
- Law, D. R., & Majewski, S. R. 2010, *ApJ*, 714, 229
- Miyamoto, M., & Nagai, R. 1975, *PASJ*, 27, 533
- Monet, D. G., Levine, S. E., Canzian, B., et al. 2003, *AJ*, 125, 984
- Navarro, J. F., Frenk, C. S., & White, S. D. M. 1997, *ApJ*, 490, 493
- Newman, J. A., Cooper, M. C., Davis, M., et al. 2013, *ApJS*, 208, 5
- Ngan, W. H. W., & Carlberg, R. G. 2015, *ApJ*, 2014, 788, 181
- Ngan, W., Carlberg, R. G., Bozek, B., Syse, R. F. G., Szalay, A. S., & Madau, P. 2016, *ApJ*, 818, 194
- Odenkirchen, M., Grebel, E. K., Rockosi, C. M., et al. 2001, *ApJL*, 548, L165
- Odenkirchen, M., Grebel, E. K., Dehnen, W., Rix, H.-W. & Cudworth, K. M. 2002, *AJ*, 124, 1497
- Odenkirchen, M., Grebel, E. K., Dehnen, W., et al. 2003, *ApJ*, 126, 2385
- Odenkirchen, M., Grebel, E., Kayser, A., Rix, H.-W., & Dehnen, W. 2009, *AJ*, 137, 3378
- Pearson, S., Küpper, A. H. W., Johnston, K., & Price-Whelan, A. M. 2015, *ApJ*, 799, 28
- Ramírez, I. & Meléndez, J. 2005, *ApJ*, 626, 465
- Reid, M. J., Menten, K. M., Brunthaler, A., et al. 2014, *ApJ*, 783, 130
- Robin, A. C., Reylé, C., Derrière, S., & Picaud, S. 2003, *A&A*, 409, 523
- Schlafly, E. F. & Finkbeiner, D. P. 2011, *ApJ*, 737, 103
- Schönrich, R., Binney, J., & Dehnen, W. 2010, *MNRAS*, 403, 1829
- Smart, R. L., 2013, *yCat*, 1324, 0
- Smith, G. H., Sneden, C. & Kraft, R. P. 2002, *AJ*, 123, 1502
- Walker & Peñarrubia. 2011, *ApJ*, 742, 20
- Yoon, J. H., Johnston, K., & Hogg, D. W. 2011, *ApJ*, 731, 58
- Zacharias, N., Monet, D. G., Levine, S. E., et al. 2005, *VizieR On-line Data Catalog*, 1297, 0